ALMA Reveals the Molecular Gas Properties of Five Star-forming Galaxies across the Main Sequence at 3

Paolo Cassata[1,2] , Daizhong Liu[3] , Brent Groves[4] , Eva Schinnerer[3] , Eduardo Ibar[5], Mark Sargent[6] , Alexander Karim[7] , Margherita Talia[8,9] , Olivier Le Fèvre[10] , Lidia Tasca[10], Brian C. Lemaux[11] , Bruno Ribeiro[12], Stefano Fiore[1], Michael Romano[1] , Chiara Mancini[1] , Laura Morselli[1] , Giulia Rodighiero[1,2] , Lucía Rodríguez-Muñoz[1] , Andrea Enia[1] , and Vernesa Smolcic[13]

[1] Dipartimento di Fisica e Astronomia, Università di Padova, Vicolo dell'Osservatorio 3, I-35122 Padova, Italy; paolo.cassata@unipd.it
[2] INAF Osservatorio Astronomico di Padova, vicolo dell'Osservatorio 5, I-35122 Padova, Italy
[3] Max-Planck-Institut für Astronomie, Königstuhl 17, D-69117 Heidelberg, Germany
[4] Research School of Astronomy and Astrophysics, The Australian National University, Canberra, ACT 2611, Australia
[5] Instituto de Física y Astronomía, Universidad de Valparaíso, Avda. Gran Bretaña 1111, Valparaíso, Chile
[6] Astronomy Centre, Department of Physics and Astronomy, University of Sussex, Brighton BN1 9QH, UK
[7] Argelander-Institut für Astronomie, Auf dem Hügel 71, D-53121 Bonn, Germany
[8] Dipartimento di Fisica e Astronomia, Universitá di Bologna, Via Gobetti 93/2, I-40129 Bologna, Italy
[9] INAF-Osservatorio Astronomico di Bologna, Via Gobetti 93/3, I-40129, Bologna, Italy
[10] Aix Marseille Université, CNRS, LAM (Laboratoire d'Astrophysique de Marseille) UMR 7326, F-13388, Marseille, France
[11] Department of Physics, University of California, Davis, One Shields Ave., Davis, CA 95616, USA
[12] Leiden Observatory, Leiden University, P.O. Box 9513, 2300 RA, Leiden, The Netherlands
[13] Department of Physics, Faculty of Science, University of Zagreb, Bijenička cesta 32, 10000 Zagreb, Croatia

Abstract

We present the detection of CO $(5-4)$ with signal-to-noise ratio (S/N) $> 7-13$ and a lower CO transition with S/N > 3 (CO $(4-3)$ for four galaxies, and CO $(3-2)$ for one) with the Atacama Large Millimeter/submillimeter Array in bands 3 and 4 in five main-sequence (MS) star-forming galaxies with stellar masses $(3-6) \times 10^{10} M_\odot$ at $3 < z < 3.5$. We find a good correlation between the total far-infrared luminosity $L_{\rm FIR}$ and the luminosity of the CO $(5-4)$ transition $L'_{\rm CO(5-4)}$, where $L'_{\rm CO(5-4)}$ increases with star formation rate (SFR), indicating that CO $(5-4)$ is a good tracer of the obscured SFR in these galaxies. The two galaxies that lie closer to the star-forming MS have CO spectral line energy distribution (SLED) slopes that are comparable to other star-forming populations, such as local submillimeter galaxies and BzK star-forming galaxies; the three objects with higher specific star formation rates have far steeper CO SLEDs, which possibly indicates a more concentrated episode of star formation. By exploiting the CO SLED slopes to extrapolate the luminosity of the CO $(1-0)$ transition and using a classical conversion factor for MS galaxies of $\alpha_{\rm CO} = 3.8\ M_\odot ({\rm K\ km\ s^{-1}\ pc^{-2}})^{-1}$, we find that these galaxies are very gas-rich, with molecular gas fractions between 60% and 80% and quite long depletion times, between 0.2 and 1 Gyr. Finally, we obtain dynamical masses that are comparable to the sum of stellar and gas mass (at least for four out of five galaxies), allowing us to put a first constraint on the $\alpha_{\rm CO}$ parameter for MS galaxies at an unprecedented redshift.

Unified Astronomy Thesaurus concepts: Star formation (1569); Interstellar medium (847)

1. Introduction

The global star formation rate density of the universe (SFRD) increased by a factor of ~ 15 in the first 3 Gyr after the big bang and then fell off by a similar factor down to the local universe (Cucciati et al. 2012; Madau & Dickinson 2014). There is a wide consensus nowadays that the bulk of the star formation activity at all epochs occurs in galaxies that lie on a relatively narrow sequence in the stellar mass versus SFR plane (main sequence, MS; Daddi et al. 2007; Noeske et al. 2007; Rodighiero et al. 2011). Galaxies were forming stars faster at earlier epochs: at $z \sim 3$ the specific star formation rates (sSFR) (SFR/$M_\odot$) of galaxies on the MS is ~ 100 times higher than that of local galaxies (Tasca et al. 2015; Faisst et al. 2016; Schreiber et al. 2016; Tomczak et al. 2016). Despite knowing when and where (i.e., mainly in $\log(M_*) \sim (3 - 10) \times 10^{10} M_\odot$ MS galaxies) the stars in the universe have formed, the mechanisms that trigger such rapid increase in the global star formation activity of the universe are still debated: is it due to an increase in the gas fraction or a higher star formation efficiency, or a combination of the two (e.g., Geach et al. 2011; Saintonge et al. 2013; Genzel et al. 2015;

Scoville et al. 2016)? In order to make significant progress, we need to link the nature of the star-forming galaxies on the MS with their gas reservoirs, eventually probing the efficiency of the star formation and the gas fraction and their evolution with cosmic time.

Although the molecular gas mass can be estimated from rather inexpensive dust continuum detections (Hildebrand 1983; Magdis et al. 2012a; Scoville et al. 2014, 2016; Groves et al. 2015), a more direct tracer of the properties of the molecular gas and of the total molecular mass is the CO line (Carilli & Walter 2013). CO detections are indeed quite standard for MS galaxies at $z < 2$ (Saintonge et al. 2011; Genzel et al. 2015; Villanueva et al. 2017; Tacconi et al. 2018), but they require increasingly longer integration times at $2 < z < 6$, the critical epoch when the SFRD of the universe experienced its accelerated growth. Therefore, in comparison to the few hundreds of MS star-forming galaxies with CO detection at $z < 1$ and the few tens that are detected at $1 < z < 3$ (Daddi et al. 2008, 2010; Genzel et al. 2015; Sharon et al. 2016; Tacconi et al. 2018), only a handful of MS galaxies at $z > 2$

have been detected in CO: Magdis et al. (2012b) obtained CO $(3-2)$ fluxes for two Lyman break galaxies at $z \sim 3$, and Saintonge et al. (2013) and Dessauges-Zavadsky et al. (2017) detected CO for four lensed MS galaxies at $2.7 < z < 3$ and one at $z \sim 3.6$ (but with additional uncertainties due to the uncertain magnification factor), respectively.

As a result, our knowledge about the interstellar medium (ISM) mass and properties at these epochs is based on submillimeter continuum detections (e.g., Schinnerer et al. 2016; Liu et al. 2019) that are subject to assumptions that are difficult to control (e.g., on the dust temperature and on the evolving metallicity at $z > 3$). In order to make progress, we observed with the Atacama Large Millimeter/submillimeter Array (ALMA), during Cycles 3 and 4, a sample of five MS galaxies at $3 < z < 3.5$ targeting two CO transitions (CO $(5-4)$ for the whole sample, CO $(4-3)$ for four galaxies, and CO $(3-2)$ for one), in order to constrain their ISM masses using the CO emission. This technique in fact relies on different assumptions (e.g., on the CO excitation state and gas density; see Narayanan & Krumholz 2014; but also again on metallicity) and therefore provides an independent estimate of ISM mass. Throughout this work, we assume $H_0 = 70$ km s^{-1} Mpc^{-1}, $\Omega_\Lambda = 0.7$, and $\Omega_M = 0.3$. We use stellar masses and SFRs based on a Chabrier initial mass function (IMF) (or converted to a Chabrier IMF, when necessary).

2. Sample and Data

We selected the galaxies for this work starting from the sample in Schinnerer et al. (2016), by choosing the five sources for which we estimated the brightest CO $(5-4)$ flux, based on their dust detections at 240 GHz in ALMA band 6, among those for which a spectroscopic redshift was available as a part of the VIMOS Ultra-Deep Survey (VUDS; Le Fèvre et al. 2015) and of the zCOSMOS Deep survey (Lilly et al. 2007).

2.1. Ancillary Data and SED Fitting

The galaxies in this sample lie in the COSMOS field, one of the most widely studied patches of the sky. Multiwavelength photometry from the UV to far-IR (FIR) rest frame, including *Galaxy Evolution Explorer*, CFHT, Subaru, VISTA, *Spitzer*, *Herschel* and Very Large Array, is available for the whole field, as part of the COSMOS survey (Capak et al. 2007; Sanders et al. 2007; Scoville et al. 2007; McCracken et al. 2012; Laigle et al. 2016). Spectroscopy is crucial to have robust and precise spectroscopic redshifts that are needed to tune the ALMA setup around the expected frequency of the CO lines: two galaxies have spectra from the VUDS (Le Fèvre et al. 2015) and three from the zCOSMOS Deep survey (Lilly et al. 2007). The published redshifts for these galaxies are based on cross-matching techniques that fit the positions of the Lyα line and of the ISM lines together, although these are almost always offset with respect to the systemic velocity by several hundred kilometers in opposite directions (Steidel et al. 2010; Marchi et al. 2019; Cassata et al. 2020). Nevertheless, with the frequency coverage of the ALMA correlator (4 GHz in each of two sidebands) the CO line is expected to fall within the covered bands using either Lyα or the ISM lines, if those are not offset with respect to the systemic velocity by more than $\sim\pm2000$ km s^{-1}. However, we also manually remeasured the spectroscopic redshifts of the five galaxies, in order to compare them with the ones derived from the CO emission. When possible, we used the detected ISM lines to fix the redshift; in

one case the ISM lines were too noisy and we used the bright Lyα emission instead.

We fitted the rich multiwavelength photometry in order to obtain physical information such as star formation rates (SFRs), stellar masses, and dust temperatures. For this work, we used the new "super-deblended" catalog by Jin et al. (2018), in which the emission in the FIR bands for each object is accurately deblended over multiple objects by using the position of the emission at shorter wavelength as a prior, in combination with UV–optical–near-IR photometry from Laigle et al. (2016). By checking the multiwavelength images, we realized that the photometry for one object, Gal2, is perturbed by a lower-redshift interloper that is not deblended in the Laigle et al. (2016) catalog; in fact, this interloper is detected in the *U*-band image, a band that at $z \sim 3$ would match the Lyman continuum. We therefore performed a band-by-band manual deblending, defining two apertures, one around the lower-redshift interloper and the other around Gal2: we estimated, band by band, the fraction of the total flux for each of the two components, and we use the deblended values to build a spectral energy distribution (SED) for Gal2.

All five galaxies are detected all the way from the UV rest frame to the 24 μm band; four out of five are also detected with *Herschel* in the FIR rest-frame (around the peak of the cold dust thermal emission at $\sim 100 \mu$m rest frame). By construction, the continuum in ALMA band 6 at 240 GHz is detected for all galaxies, and we included it in the SED fitting along with the continuum in band 4, which we obtained as a part of this project (see the next section for details). We fitted the multiband photometry with MAGPHYS (da Cunha et al. 2008), with the redshift fixed to the spectroscopic one, and including the photometric point from the ALMA band 4 and 6 continuum observations. MAGPHYS fits the whole multi-wavelength SED from the UV to the FIR/submillimeter, ensuring the balance between the energy absorbed by the dust in the UV and that reemitted in the FIR. As outputs of the fitting procedure, MAGPHYS provides stellar masses, SFRs, and total FIR luminosities $L_{\rm FIR}$, among others. The galaxies turn out to be quite massive, with stellar masses in the range $3 \times 10^{10} < M_*/M_\odot < 8 \times 10^{10}$, and star-forming, with SFR $\sim$ 100–600$M_\odot$ yr^{-1}. As a check, we then derived the obscured SFR from the total FIR luminosities using the classical Kennicutt (1998) conversion, assuming a Chabrier IMF; this should be a good proxy of the total SFR, since all five objects are quite obscured at UV rest-frame wavelengths. However, we obtain from the FIR SFR $\sim$ 200–2000 $M_\odot$ yr^{-1}, in all cases larger, by a factor of 1.5–3.5, than the ones obtained from MAGPHYS. This is not completely unexpected, as old stellar populations can also heat up the dust in the ISM (da Cunha et al. 2010), and our galaxies are already quite massive at $z \sim 3$, implying an underlying population of old stars, on top of which new stars are forming. Therefore, we consider the SFRs from MAGPHYS more robust, and we prefer them in the remainder of the paper, but, to be conservative, we also show how the results would change should the Kennicutt law be used to compute the SFR. Coordinates, redshifts, stellar masses, SFRs, FIR luminosities, dust temperatures, and distances from the MS $\delta_{\rm MS} = {\rm sSFR/sSFR(MS)}$ are summarized in Table 1.

From both photometry and spectroscopy, the five objects have all the properties typical of normal star-forming galaxies: Lyα is bright in one galaxy while very weak or in absorption in the other four; ISM features such as O I, C II, C IV, and Si IV are

Table 1
General Properties of the Sample

	R.A.	Decl.	z_{spec}	$\log(M_*)$ $(M_\odot)$	$\log(SFR)$[a] $(M_\odot \, yr^{-1})$	$\log(L_{FIR})$ $(L_\odot)$	T_{dust} (K)	δ_{MS}[b]
Gal1	10:01:23.182	+02:36:26.06	3.1120[c]	10.86	2.49(2.73)	12.73	54.1 ± 6.3	1.34(2.40)
Gal2	09:59:38.292	+02:13:19.93	3.0494[c]	10.82	2.17(2.30)	12.30	30.7 ± 2.4	0.69(0.94)
Gal3	10:01:19.546	+02:09:44.53	2.9342[c]	10.49	2.53(2.71)	12.71	39.8 ± 1.0	3.11(4.79)
Gal4	10:01:06.802	+02:15:31.74	3.4388[d]	10.82	2.80(3.33)	13.33	62.1 ± 1.3	2.94(10.14)
Gal5	09:59:30.523	+02:17:01.95	3.3428[c]	10.80	2.86(3.00)	12.82	54.2 ± 2.7	3.41(4.80)

Notes.
[a] The first value is the SFR estimated by MAGPHYS; the one in parentheses is based on L_{FIR}.
[b] Defined as sSFR/sSFR(MS); first value based on MAGPHYS, the one in parentheses on L_{FIR}.
[c] Based on ISM lines.
[d] Based on Lyα.

observed in absorption; and there is no evidence of active galactic nucleus (AGN) features in the observed optical spectra or of a warm torus in the broadband photometry.

In Figure 1 we show their sSFR, relative to the sSFR of galaxies on the MS sSFR(MS), defined using the MS presented by Schreiber et al. (2015) at the median redshift of $z = 3$) as a function of redshift, in comparison with similar samples of star-forming galaxies at $z > 1$ that have at least one CO transition detected in the submillimeter. The figure is built readapting Figure 1 from Villanueva et al. (2017) and Genzel et al. (2015), which used a slightly different parameterization of the MS, valid only up to $z \sim 2.5$, by Whitaker et al. (2012): in any case, the two parameterizations do not differ too much in the stellar mass range spanned by the galaxies in this work; therefore, the different samples can be compared consistently. From Figure 1, the region ± 0.6 dex around the MS is explored quite well up to redshift 2.5 by the galaxies from the PHIBBS 1 and 2 samples (Tacconi et al. 2010, 2013; Combes 2016) and by the samples presented in Magnelli et al. (2012), Daddi et al. (2010), and Magdis et al. (2012b). Submillimeter galaxy (SMG) samples from Greve et al. (2005), Tacconi et al. (2006, 2008), and Bothwell et al. (2013) span a higher range of sSFR, typically 0.6 dex above the MS. Only a handful of galaxies have CO detections at $z > 3$: two galaxies from Daddi et al. (2010) and Magdis et al. (2012b), three SMGs, and two lensed galaxies. For each galaxy in our sample we show in Figure 1 the two sSFRs obtained from MAGPHYS and from rescaling the FIR luminosity (filled and open yellow stars, respectively). It can be seen that our five galaxies span the upper half of the classical MS (sSFR $< 4 \times$ sSFR(MS); Rodighiero et al. 2011, 2014; Elbaz et al. 2018); however, two galaxies (Gal1 and Gal2) lie very close to the MS, while the other three sit close to the line that marks the transition between MS and starburst population (the SFR from MAGPHYS gives sSFR $< 4 \times$ sSFR(MS), but the SFR from the FIR gives sSFR $> 4 \times$ sSFR(MS)).

2.2. ALMA Data

The five galaxies in the sample were observed in ALMA Cycle 3 (2015.1.01590.S; PI: Cassata) in band 3 (around 110 GHz, configuration C40-5) and band 4 (around 140 GHz, configuration C40-4) between 2016 June 9 and 2016 July 31 (plus a repetition of a failed observation on 2016 October 29) to target two CO transitions for each galaxy: CO (5−4) for all galaxies (in band 4), CO (4−3) for four galaxies, and CO (3−2) for one (in band 3). The time spent on-source ranges from a few minutes to 25 minutes per object per band. Standard
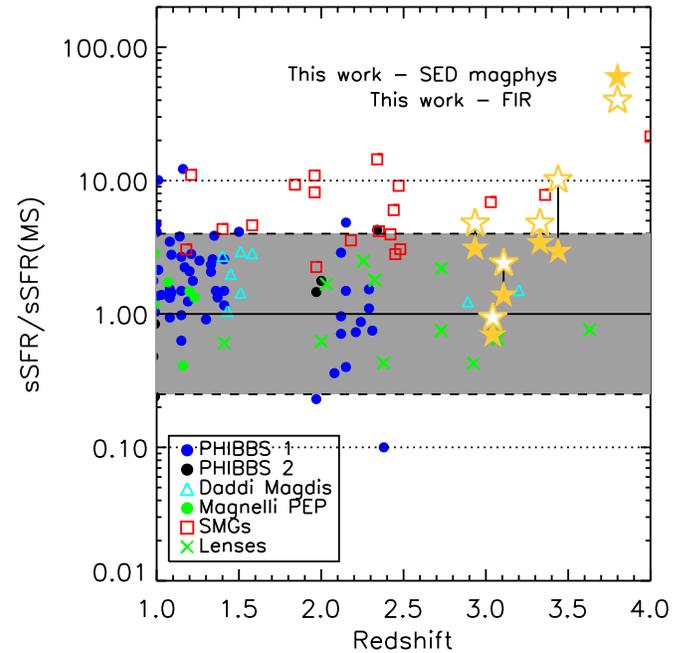

Figure 1. sSFR, normalized to the one estimated for the MS (sSFR(MS)) as a function of redshift, for different samples of normal "MS" galaxies with at least one CO line detected in their spectra. Blue and black circles show, respectively, galaxies from the PHIBBS 1 survey (Tacconi et al. 2010, 2013) and PHIBBS 2 survey (Combes 2016); red squares indicate SMGs from Greve et al. (2005), Tacconi et al. (2006, 2008), and Bothwell et al. (2013); cyan triangles indicate star-forming BzK objects from Daddi et al. (2010) and Magdis et al. (2012b); filled green circles are galaxies from Magnelli et al. (2012); and green crosses indicate lensed galaxies from Saintonge et al. (2013) and Dessauges-Zavadsky et al. (2017). Yellow stars show the five objects presented in this work: filled stars indicate the SFR that is obtained by the MAGPHYS tool; open stars indicate the SFRs that are obtained converting the L_{FIR} using the classical Kennicutt relation. The horizontal solid line marks the location of the MS; the dashed (dotted) lines indicate the loci $4 \times$ ($10 \times$) times above or below the MS. The gray area emphasizes the location of the MS, according to the classical definition by Rodighiero et al. (2011, 2014) and Elbaz et al. (2018).

sources J1058+0133, J0948+0022, and Titan were used for calibration.

The data analysis has been carried out with standard analysis pipelines available as part of CASA version 4.7 (McMullin et al. 2007). The cubes were cleaned and imaged adopting a natural weighting scheme, which maximizes the sensitivity to faint signal, and using masks at source position and setting a threshold of $3 \times$ rms noise level on the dirty images, which was measured to range from ~ 0.35 to ~ 0.95 mJy beam^{-1}. Although the natural

Table 2
Properties of the ALMA Observations

	Beam Band 3 (arcsec × arcsec)	Beam Band 4 (arcsec × arcsec)	ToS[a] Band 3 (minute)	ToS Band 4 (minute)	rms[b] Band 3 (mJy beam^{-1})	rms[b] Band 4 (mJy beam^{-1})
Ga11	0.61 × 0.85	0.76 × 1.48	21.17	9.58	0.47	0.40
Ga12	0.61 × 0.85	0.76 × 1.48	21.17	9.58	0.73	0.50
Gal3	0.73 × 0.92	0.81 × 1.08	3.53	4.54	0.95	0.65
Gal4	0.61 × 0.64	0.6 × 0.72	11.59	25.20	0.58	0.34
Gal5	0.61 × 0.64	0.6 × 0.72	11.59	25.20	0.63	0.34

Notes.
[a] Time on-source.
[b] The rms are calculated, in channels of 40 km s^{-1}, with the CASA tool IMSTAT in the cubes that are the result of the CLEAN process, described in the text.

resolution of the data is $\sim$20 km s^{-1}, we extracted the cubes in spectral bins of 40 km s^{-1}, which is more than enough to resolve lines that have spectral FWHM in excess of 200 km s^{-1}. The resulting clean beams have FWHM $\sim$ 0″6–1″ (elliptical in a few cases). The clean beam sizes, on-source times, and noise levels of each image are reported in Table 2: it can be seen that for Gal1 and Gal2 the beams in band 3 are quite smaller than those in band 4; for each of the other 3 galaxies the beam size in band 3 matches quite well that in band 4. The largest recoverable angular scales are 6″7 and 7″5 for band 3 and band 4 observations, respectively, and therefore these configurations are appropriate to retrieve the total flux from objects that have diameters of the order of 2″–3″.

Initially, CO spectra are extracted from a circular region with 2″ diameter around the positions of the expected emission. This first step is only used to identify the channels to integrate to obtain the moment 0 maps: we selected the channels above 1σ of the cube rms bracketing the peak of the line emission. We then collapsed the cubes into moment 0 maps, with the *immoments* task. Continuum maps are instead obtained collapsing the three out of four sidebands not containing the CO emission. The maps are presented in Figure 2, together with a *Hubble Space Telescope* (*HST*) image in the F814W filter from the COSMOS project (Koekemoer et al. 2007; Scoville et al. 2007). In order to obtain the total line and continuum fluxes, we first built a segmentation map, in which we keep all the pixels contiguous to the center in which the measured flux is above 2σ (measured in a region not containing the source), after subtracting the continuum; we then integrate the flux from these pixels. This method includes less (noisy) pixels than a classical aperture photometry approach and therefore maximizes the signal-to-noise ratio (S/N) of the measurements. Whenever the emission region is smaller than the clean beam, and therefore the emission is not resolved, we take the peak flux as the total flux.

Finally, we re-extracted the spectra from the same regions in the moments 0 maps that have signal 2σ over the rms: the spectra are shown in Figure 3, centered in velocity on the peak of the CO (5−4) line. CO (5−4) emission is well detected in all five objects, with FWHM between $\sim$150 (Gal1) and $\sim$600 km s^{-1} (Gal4). The shapes of the line profiles are quite diverse: from a narrow line (Gal1) to a double peak (Gal3) to broad emission (Gal2, Gal4, and Gal5). The second line, in band 3, is also detected in all objects, although with lower significance. It is important to stress that these spectra have shapes that are very similar to the ones extracted in the first step; however, they are less noisy than those, having been extracted only from the region where the line signal is robustly detected.

3. CO versus Dust Continuum versus UV

We detect CO (5−4) emission at $\geqslant$7σ for all five objects (and up to 13σ for object 4), while CO (4−3) (and CO (3−2) for gal 3) emission is detected at $\geqslant$3σ for all objects (see Table 3). The continuum in band 3 at $\sim$650 μm rest frame is not detected (therefore not shown in Figure 2), while the continuum in band 4 at $\sim$500 μm rest frame is always detected at $\geqslant$4σ (therefore we included it in the SED fitting process presented in Section 2.1). We obtain line-integrated fluxes L_{CO} in the range 0.4–1 Jy km s^{-1} for CO (4−3) (or CO (3−2) for object 3) and 0.6–3 Jy km s^{-1} for CO (5−4). We checked that these values are within ±10% from the values obtained by using the GAUSSFIT or 2DFIT tool within CASA.

In the first two panels for each galaxy in Figure 2 we show the comparison between the positions of the two CO emissions (blue and red) of the dust (green) and of the UV–optical rest-frame light (gray scale, as traced by the *HST*/F814W and UltraVISTA K_s DR4 imaging, corresponding to $\sim$2000 Å and $\sim$5000 Å rest frame, respectively). In Figure 2 we report as well the position of the spectral slit, in order to compare the regions where the CO, dust, and optical spectrum originate for each galaxy.

3.1. Gal1

The morphology of Gal1 in the Advanced Camera for Surveys (ACS)/z band (corresponding to 2000 Å rest frame) appears quite faint and compact, and the UltraVISTA DR4 K_s image, corresponding to the 5500 Å rest frame, shows also a quite compact morphology, aligned within 0″1 with the ACS/z-band one (see Figure 2. The ALMA band 4 continuum emission is not spatially resolved and falls on top of the z-band/K_s emission. The spectroscopic slit is well aligned with the UV–optical–ALMA emission, and Gal1 has a spectroscopic redshift z_{opt} = 3.1120, based on the Si II λ1260.4, O I λ1303, [C II] λ1334.5, Si IV λ1393.8+Si IV λ1402.8, and Si II λ1526.7 lines detected in the VUDS spectrum. Both CO emission lines are quite narrow, with FWHM $\sim$ 200 km s^{-1} (see Figure 3), and they are centered at z_{CO} = 3.1181, meaning that the ISM is blueshifted with respect to the CO lines by $\sim$400 km s^{-1}. If we assume that the CO is a good tracer of the systemic velocity of the system, this implies that the ionized gas traced by the UV ISM lines is outflowing with velocities $\sim$400 km s^{-1}, not unusual for galaxies at these redshifts (Steidel et al. 2010; Erb et al. 2014; Marchi et al. 2019). We can conclude that this is very likely a single object, with dust that, along some line of sight, absorbs the UV light, re-emitting it in the FIR. By fitting the multiwavelength photometry from the UV to submillimeter, we derive a stellar mass of $M_* = 7.25 \times 10^{10}\ M_\odot$
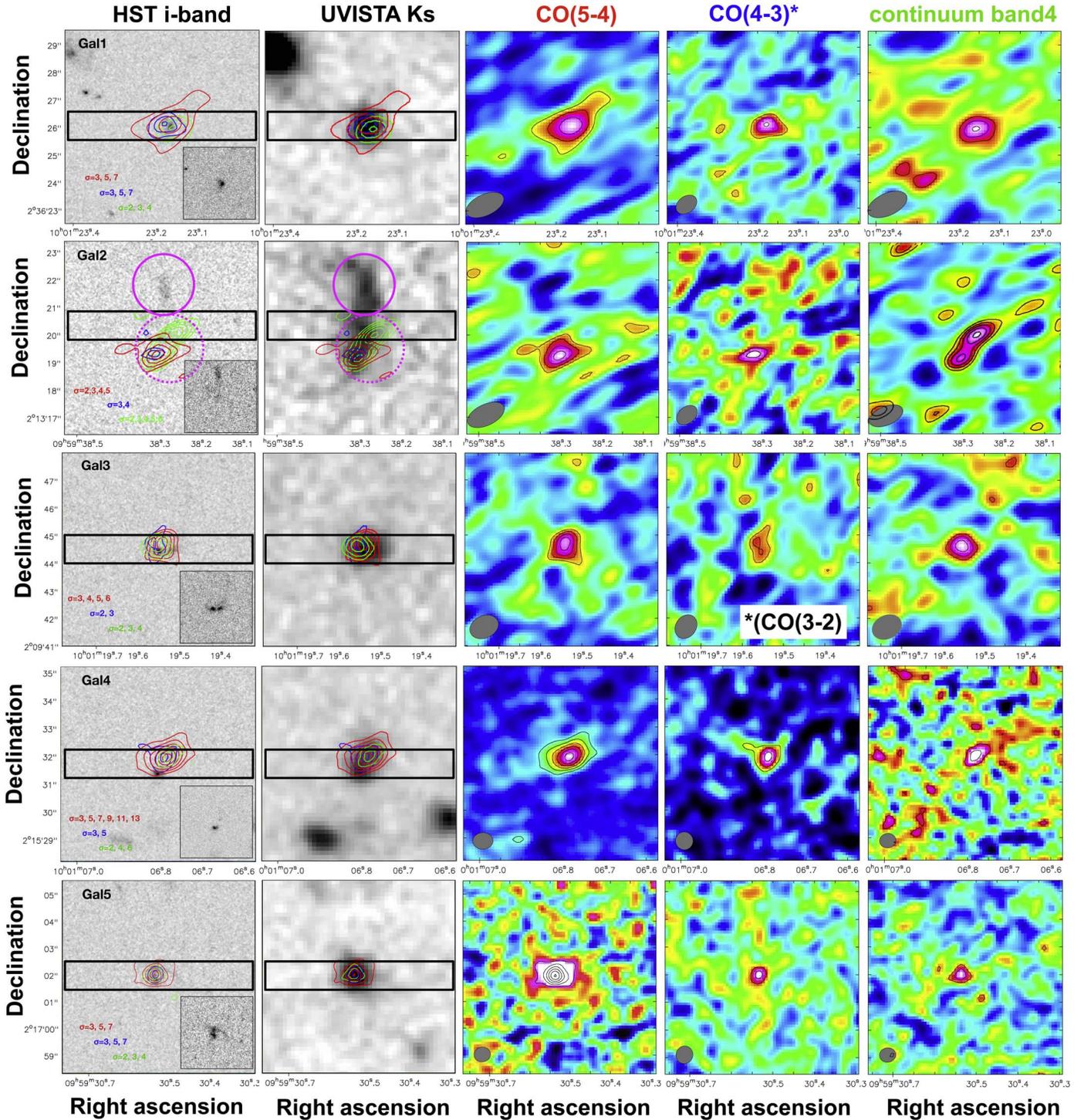
Figure 2. For each galaxy in the sample, we show, from left to right, the *HST*/F814W image from the COSMOS survey (Koekemoer et al. 2007; Scoville et al. 2007), the K_s image from the UltraVISTA DR4 release (McCracken et al. 2012), and images overlaid with the contours of the CO (5−4) line (in red), the CO (4−3) or CO (3 −2) (in blue), and the continuum in band 4 (in green); the CO (5−4) map in band 4; the CO (4−3) or CO (3−2) map in band 3; and the continuum image in band 4 at ~500 μm. For the ALMA images, we used a natural weighting scheme, which maximizes the sensitivity of the maps; only for the band 4 continuum map of Gal2 did we use a Briggs weighting scheme, to resolve the extended emission. See text for details. The contours show increasing S/N steps, as indicated in each panel. The *HST* image is repeated, on the left, for each object, in a smaller panel without ALMA contours, in order to better show the UV rest-frame morphology. In the first two panels of each object the black rectangle shows the position of the spectroscopic slit.

and a $\delta_{MS} = 1.38$ (or $\delta_{MS} = 2.4$, if the FIR is used to estimate the SFR).

The peaks of the CO (5−4), CO (4−3), and continuum in band 4 are within $0\rlap{.}''5$ of each other and on top of the position of the UV–optical rest-frame emission, as traced by the *HST*/F814W

and UltraVISTA K_s images. Both CO lines are spatially resolved, as can be seen in Figure 2. In band 4, the CO (5−4) emission has a size (deconvolved from beam) of $1\rlap{.}''66 \pm 0\rlap{.}''48$ (major axis) $\times$ $0\rlap{.}''74 \pm 0\rlap{.}''23$ (minor axis), with a clean beam of $1\rlap{.}''48 \times 0\rlap{.}''76$.
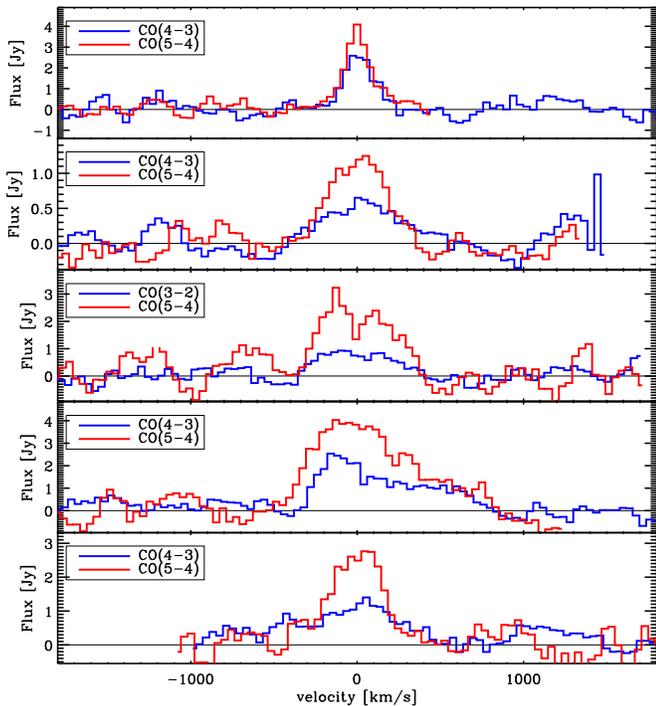
Figure 3. Millimeter/submillimeter spectra of the five sample galaxies in band 4 (red) and band 3 (blue), highlighting, respectively, the CO (5−4) emission and the CO (4−3) (for objects 1, 2, 4, and 5) or CO (3−2) (for object 3). The spectra, extracted in channels of 40 km s^{-1}, are expressed in Jy as a function of the velocity offset from the redshift centered on the CO (5−4) line and are extracted from the region over which we integrate the moment 0 maps to obtain the total line fluxes. In each panel, we report the FWHM of the CO (5−4) line emission.

3.2. Gal2

This is the object for which the multiwavelength photometry is perturbed by a lower-redshift interloper. In Figure 2 we show the two circular apertures that we used to deblend the two components: the interloper and the actual object at $z \sim 3$ are shown by the solid line and dotted line, respectively. Gal2 is very faint in the ACS/z band (corresponding to 2000 Å rest frame) and shows a quite irregular and extended morphology in the optical rest frame, probed by the UltraVISTA K_s band. In particular, the object extend for $\sim 2\rlap{.}''5$ (~ 20 kpc at $z \sim 3$) perpendicularly to the spectroscopic slit. The CO (5−4) and CO (4−3) emissions are spatially unresolved, coincident with each other, but offset from the band 4 continuum emission, which is quite extended (see Figure 2): we could measure a size of $1\rlap{.}''934 \pm 0\rlap{.}''350$ (FWHM along the major axis, corresponding to 15.0 ± 2.5 kpc) $\times 0\rlap{.}''767 \pm 0\rlap{.}''060$ (FWHM along the minor axis, corresponding to 6.0 ± 0.5 kpc), under a clean beam of $\sim 1.47 \times 0\rlap{.}''76$. In order to investigate this further, we performed a different cleaning process only for this object, using this time a Briggs weighting scheme (Briggs 1995) with *robust* parameter 0.5, in order to improve the spatial resolution, without compromising too much the sensitivity. With this imaging, it appears that the band 4 continuum emission is actually bimodal, with a peak that is spatially coincident with the CO lines and a second component that is aligned NW with respect to the first one, and lying within the spectroscopic slit.

For this object, the CO emission is much less extended than the optical rest-frame light traced by the UltraVISTA K_s imaging; moreover, the CO emission is also spatially offset from the spectroscopic slit, meaning that it originates from a

region that is not probed by the optical spectroscopy. The spectroscopic redshift, recentered on the ISM lines (based on the Si II λ1260.4, O I λ1303, Si II λ1526.7, and C IV λ1548.4 lines), turns out to be $z_{opt} = 3.0494$, offset by -450 km s^{-1} with respect to the CO emissions, which are quite broad (FWHM ~ 350–500 km s^{-1}) and centered at $z_{CO} = 3.0557$. It is worth noting that the ALMA tuning could reveal CO (5−4) between $z = 3.0204$ and $z = 3.12535$; therefore, it could detect emission offset from the optical emission by -6000 up to $+1850$ km s^{-1}: the fact that the CO (5−4) is not detected in the region overlapping with the spectroscopic slit means that there is no (or very little, not detectable) CO in that region.

When we fit the multiwavelength deblended photometry for Gal2 with MAGPHYS, we obtain a stellar mass of $M_* = 6.6 \times 10^{10} \, M_\odot$ and a $\delta_{MS} = 0.69$ (or $\delta_{MS} = 0.94$, if the FIR is used to estimate the SFR).

3.3. Gal3

The morphology of Gal3 in the UV rest frame (traced by the ACS/i-band image) is quite irregular: a bright clump sits aside with a fainter and smoother component, separated by $\sim 0\rlap{.}''7$. The object looks more regular in the UltraVISTA DR4 K_s image, corresponding to the optical 5500 Å rest frame, and the emission is centered between the two UV rest-frame peaks. The continuum emission in band 4 is not spatially resolved and lies on top of the brightest UV peak, within $\sim 0\rlap{.}''3$ from the optical rest-frame emission.

The spectroscopic slit is well aligned with the UV–optical– ALMA emission, and the object has a spectroscopic redshift $z_{opt} = 2.9342$, based on the Si II λ1260.4, O I λ1303, [C II] λ1334.5, Si II λ1526.7, and C IV λ1548.4 lines, revealed in the zCOSMOS spectrum. Both CO emission lines are quite broad, with FWHM ~ 400–450 km s^{-1} (see Figure 3), with the CO (5−4) line being clearly double peaked, with the two peaks separated by 250 km s^{-1}, possibly indicating a rotating disk, and centered at $z_{CO} = 2.9348$, which implies that the ISM lines are blueshifted with respect to the CO by 45 km s^{-1}, a difference that is not statistically significant, given the precision of the optical spectroscopy, which provides a resolution of ~ 100 km s^{-1}. Since the spatial and spectral offsets we find are small or absent, we can conclude that this is a single object. Running MAGPHYS, we obtain for Gal3 a stellar mass of $M_* = 3.1 \times 10^{10} \, M_\odot$ and a $\delta_{MS} = 3.1$ (or $\delta_{MS} = 4.7$, if the FIR is used to estimate the SFR).

The CO (5−4) emission is spatially resolved, but both the CO (3−2) emission and the continuum in band 4 are not. In particular, we could measure a size of $1\rlap{.}''92 \pm 0\rlap{.}''55$ (FWHM along the major axis, corresponding to $\sim 15 \pm 4$ kpc) $\times 0\rlap{.}''43 \pm 0\rlap{.}''40$ (FWHM along the minor axis, corresponding to $\sim 3.3 \pm 3$ kpc), for a clean beam of $1.08 \times 0\rlap{.}''81$. The peaks of the two CO lines and the continuum emission are within $0\rlap{.}''2$ from each other, they are offset by $\sim 0\rlap{.}''2$ from the position of the UV emission, as revealed by the ACS/i-band imaging, and they are coincident with the optical emission, traced by the K_s imaging.

3.4. Gal4

The morphology of Gal4 in the ACS/i band, corresponding to the UV rest frame, is double peaked, as it is the morphology in the UltraVISTA DR4 K_s imaging, which matches the optical rest frame: both peaks fall within the $1''$ spectroscopic slit and are separated by $\sim 0\rlap{.}''7$. The ALMA band 4 emission is not

Table 3
Measurements on ALMA Data for the Sample

	z_{CO}	$L_{CO(4-3)}\Delta v$ (Jy km s^{-1})	$L_{CO(5-4)}\Delta v$ (Jy km s^{-1})	F(band4) (μJy)	σ_e[a] (Km s^{-1})	D[b] (kpc)
Gal1	3.1181	0.58 ± 0.06	0.71 ± 0.05	132 ± 32	83	14.48 ± 1.52
Gal2	3.0557	0.50 ± 0.11	0.52 ± 0.11	212 ± 29	161	8.28 ± 1.30
Gal3	2.9348	0.47 ± 0.16[a]	1.28 ± 0.16	237 ± 43	193	10.08 ± 1.16
Gal4	3.4315	1.10 ± 0.12	2.90 ± 0.08	111 ± 22	279	9.58 ± 0.59
Gal5	3.3411	0.73 ± 0.13	1.09 ± 0.06	156 ± 23	158	8.35 ± 0.52

Notes.
[a] Standard deviation, or dispersion, of the Gaussian that fits the line profile; the FWHM can be obtained as FWHM = $\sigma_e \times$ 2.35.
[b] Deconvolved from the instrumental beam.

spatially resolved and is centered on top of the faintest of the two peaks revealed by the i/K_s-band imaging. This might indicate that the dust is not homogeneously distributed in this object: the UV-bright clump indicates a region free of dust, from which the UV photons are free to escape; the region where the ALMA band 4 continuum is emitted is, on the other hand, rich of dust that absorbs the UV photons and reemits them in the FIR/submillimeter. The spectroscopic slit is well aligned with the UV–optical–ALMA emission, and the object has a spectroscopic redshift $z_{opt} = 3.4388$, based in this case on the peak of the Lyα line (the ISM absorption lines are in this case very faint).

Both CO emission lines are very broad, with FWHM ~ 500 km s^{-1} (see Figure 3), have an asymmetric shape, with the lines being skewed for high velocities, and are centered at $z_{CO} = 3.4315$. This implies that the Lyα emission is redshifted with respect to the CO by ~500 km s^{-1}, not unusual for galaxies at these redshifts (Steidel et al. 2010; Erb et al. 2014; Marchi et al. 2019). We can conclude, again, that, since the spatial offsets between UV–optical and FIR/submillimeter are small, and there is no evidence of other components from the optical and ALMA spectra, Gal4 is a single object. Running MAGPYS on the multiwavelength photometry provides for Gal4 a stellar mass of $M_* = 6.6 \times 10^{10} M_\odot$ and a $\delta_{MS} = 3$ (or $\delta_{MS} = 10$, if the FIR is used to estimate the SFR).

The CO (5−4) emission is spatially resolved, and the CO (4−3) emission is marginally resolved, while the continuum emission in band 4 is unresolved. We could measure a size of $1''.315 \pm 0''.156$ (FWHM along the major axis, corresponding to 10 ± 1.15 kpc) $\times$ $0''.606 \pm 0''.094$ (FWHM along the minor axis, corresponding to 4.5 ± 0.7 kpc), under a clean beam of $0''.73 \times 0''.60$, for the CO (5−4) emission. As can be seen from Figure 2, the CO (5−4), CO (4−3), and band 4 continuum all sit on top of each other, and the emissions are coincident with the center of the map, where the multiwavelength photometry and the spectrum were extracted. The ALMA continuum and CO emissions are offset by ~$0''.8$ from the brightest clump detected in the UV–optical rest frame, probed by the *HST* i-band and UltraVISTA K_s images.

3.5. Gal5

The morphology of Gal5 is quite irregular in the ACS/i-band imaging, tracing the UV rest frame, with a bright clump and a faint feature, which could resemble a tidal tail, separated by $0''.5$. Gal 5 is, on the other hand, more regular in the UltraVISTA DR4 K_s imaging, which traces the optical rest frame, with the emission lying right on top of the UV light. The continuum in ALMA band 4 is not spatially resolved and is well aligned with the UV and

optical rest-frame emission. The spectroscopic slit is well aligned with the UV–optical–ALMA light, and the object has a spectroscopic redshift $z_{opt} = 3.3428$, based on Lyα λ1215.7 in absorption, Si II λ1260.4, Si IV λ1393.8 + Si IV λ1402.8, Si II λ1526.7, and C IV λ1549.5 lines. Both CO emission lines are quite broad, with FWHM ~ 400–700 km s^{-1} (see Figure 3), and centered at $z_{CO} = 3.3411$, implying an offset between ISM lines and CO of +100 km s^{-1}, not statistically significant owing to the quite low spectral resolution provided by the VUDS spectroscopy. Again, this indicates that this is very likely a single object. Running MAGPHYS on the multiwavelength photometry, we obtain a stellar mass of $M_* = 3.7 \times 10^{10} M_\odot$ and a $\delta_{MS} = 3.3$ (or $\delta_{MS} = 4.9$, if the FIR is used to estimate the SFR).

The CO (5−4) emission is spatially resolved, while the CO (4−3) emission is not. We could measure a size of $0''.998 \pm 0''.143$ (FWHM along the major axis, corresponding to 7.5 ± 1.1 kpc) $\times$ $0''.566 \pm 0''.101$ (FWHM along the minor axis, corresponding to 4.2 ± 0.75 kpc), under a clean beam of $0.62 \times 0''.55$, for the CO (5−4) emission. As can be seen from Figure 2, the CO (5−4), CO (4−3), and band 4 continuum all sit on top of each other, and they are coincident with K_s emission, which is at the center of the map.

4. CO Luminosity and SLED Slope

We obtain CO (5−4) luminosities from the fluxes by applying the following equation from Solomon et al. (1992):

$$L'_{CO(5-4)} = 3.25 \times 10^7 \times S_{CO(5-4)}\Delta v$$
$$\times \frac{D_L^2}{(1+z)^3 \nu_{obs}^2} \text{K km s}^{-1} \text{ pc}^2, \quad (1)$$

where $S_{CO(5-4)}\Delta v$ is the velocity-integrated line flux, D_L is the luminosity distance, ν_{obs} is the observed frequency of the emission, and z is the redshift.

We report in Table 4 the CO (5−4) luminosities L'_{CO}, and in Figure 4 we plot them against L_{FIR}, in comparison with data from literature, including local SMGs and ULIRGs by Magdis et al. (2012a) and Carilli & Walter (2013) and BzK galaxies at $z \sim 1.5$ by Daddi et al. (2015). Our objects are at the high end of the distribution of points, and they distribute quite well around the linear correlation proposed by Daddi et al. (2015). It is interesting to note that the two galaxies that lie closer to the average MS at $z \sim 3$, Gal1 and Gal2, have also the smallest $L'_{CO(5-4)}$. Our measurements therefore confirm that the correlation between the CO (5−4) line and FIR luminosities, observed at $z \sim 0$ and $z \sim 1.5$, is still in place at $z > 3$ for MS galaxies.

Table 4
Derived Properties of the Sample from ALMA Data

	$L'_{CO(5-4)}$ $(10^{10} \text{ K km s}^{-1} \text{ pc}^2)$	$M_{gas,CO}$ $(10^{10}\, M_\odot)$	$M_{gas,\, band4}$ $(10^{10}\, M_\odot)$	$\mu_{gas,CO}$ [a]	$\mu_{gas,band4}$ [a]	$t_{depl,CO}$ (Gyr)	$t_{depl,band4}$ (Gyr)	M_{dyn} $(10^{11}\, M_\odot)$
Gal1	1.20 ± 0.20	13.52 ± 1.35	11.87 ± 2.87	0.66	0.63	0.44	0.39	0.47 ± 0.06
Gal2	8.39 ± 0.18	9.48 ± 2.01	19.21 ± 2.64	0.59	0.74	0.64	1.29	1.09 ± 0.19
Gal3	1.95 ± 0.24	10.29 ± 1.28	19.00 ± 3.41	0.77	0.86	0.31	0.56	1.80 ± 0.23
Gal4	5.74 ± 0.57	21.79 ± 2.18	8.34 ± 1.65	0.77	0.56	0.35	0.13	3.57 ± 0.29
Gal5	2.05 ± 0.20	10.84 ± 1.08	11.68 ± 1.76	0.63	0.65	0.15	0.16	1.47 ± 0.14

Note.
[a] Defined as $M_{gas}/(M_{gas} + M_*)$.
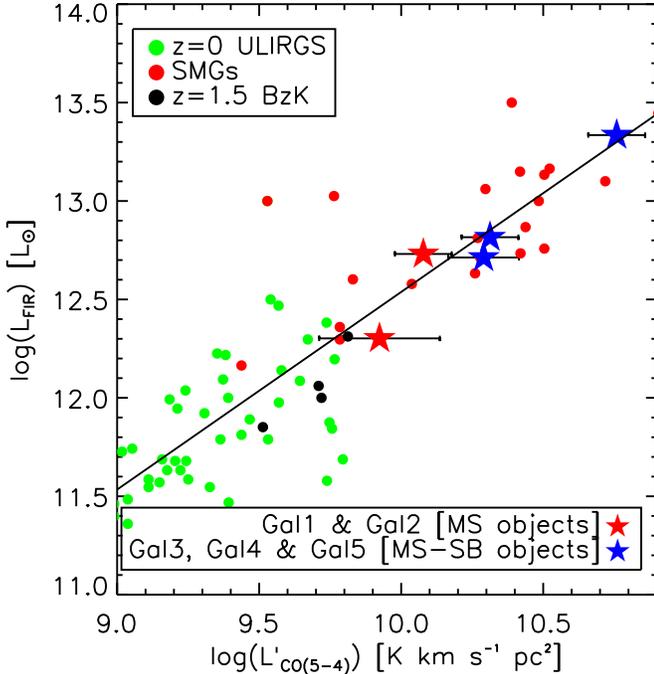
Figure 4. FIR luminosity, obtained with MAGPHYS from fitting the SED, as a function of CO (5−4) luminosity $L'_{CO(5-4)}$, for the five galaxies in our sample (red stars: normal MS galaxies; blue stars: galaxies at the boundary to starbursts), together with literature data points (compilation by Daddi et al. 2015: green and red circles are $z = 0$ ULIRGs and SMGs, respectively, from Magdis et al. 2012a; Carilli & Walter 2013; black circles are BzK galaxies at $z \sim 1.5$ by Daddi et al. 2015). The diagonal line is the linear correlation proposed by Daddi et al. (2015).

The shape of the CO SLED can be used to investigate the nature of galaxies by constraining properties of the energy source that excites the ISM (Carilli & Walter 2013). In Figure 5 we compare the CO SLED slope between CO (5−4) and CO (4−3), defined as $SL_{5/4} = S_{CO(5-4)}/S_{CO(4-3)}$, for the five galaxies in this sample, as a function of $L'_{CO(5-4)}$ and δ_{MS}, with values for various types of galaxies in the literature.

Since for Gal3 we targeted and observed CO (3−2) instead of CO (4−3), for that object we linearly interpolate the CO (5−4) and CO (3−2) fluxes to obtain $S_{CO(4-3)}$. By looking at Figure 5, it is clear that Gal1 and Gal2, the objects that lie closer to the MS, have CO SLED slopes that are compatible with those of various classes of star-forming galaxies, such as local ULIRGs (Papadopoulos et al. 2012), BzK at $z \sim 1.5$ (Daddi et al. 2015), SMGs (Bothwell et al. 2013), and QSOs (Carilli & Walter 2013); these two objects are also the ones with the lowest $L'_{CO(5-4)}$ luminosities. On the other hand, Gal3,

Gal4, and Gal5, those that lie close to the boundary between the MS and starbursts (SBs) and that have the highest $L'_{CO(5-4)}$ luminosities, have much steeper CO SLED slopes, in one case even in excess of those expected for a constant brightness temperature on the Rayleigh–Jeans scale, i.e., $S \propto \nu^2$. It is important to stress that none of the five galaxies in this sample show signs of the presence of an AGN, at any wavelength. A Spearman correlation test ($r_S = 0.9$) confirms that a positive correlation exists between the $SL_{5/4}$ parameter and $L'_{CO(5-4)}$. We checked that the $SL_{5/4}$ parameter does not correlate with other parameters, such as gas or stellar mass, continuum luminosity, or source size, but shows a similar correlation to sSFR (right panel of Figure 5). This indicates that $SL_{5/4}$ also correlates with L_{FIR} and therefore star formation. It is also significant that we do see a correlation between distance from the MS and the dust temperature fitted by MAGPHYS: Gal4 and Gal5, which are more offset from the MS and have higher $SL_{5/4}$ and $L'_{CO(5-4)}$, have higher dust temperatures, in excess of 50 K (see Table 1), while the other three galaxies have temperatures around 35 K (except for Gal1, for which, however, the temperature is not very well constrained).

5. Gas Masses from CO and Band 4 Continuum

As we discussed in Section 1, both CO lines and the dust continuum in the Rayleigh–Jeans regime can be used as tracers for the molecular gas (e.g., Genzel et al. 2015; Scoville et al. 2016). In this section we present and compare the gas masses determined using the two methods.

In order to obtain an estimate of the molecular gas mass from our CO measurements, we have to make two assumptions: the first is about the flux ratio between the CO (5−4) and CO (1−0) transitions; the second assumption is about the α_{CO} conversion factor between the CO (1−0) luminosity and the molecular gas mass (for a review see Bolatto et al. 2013). Although extrapolating the CO (1−0) luminosity from the CO (5−4) one can be tricky (see Carilli & Walter 2013; Daddi et al. 2015), in our case we have the advantage that we detect a second lower transition for all objects, which we use to obtain at least a first guess on the overall shape of the CO SLED. By using the values presented in Section 4, and in particular in Figure 5, we calibrate the flux ratios between CO (5−4) and CO (1−0) for the five galaxies in our sample: for Gal4, the one with the most extreme slope, we use $L'_{CO(5-4)}/L'_{CO(1-0)} = 25$; for Gal3 and Gal4, both of which have intermediate slopes, we use $L'_{CO(5-4)}/L'_{CO(1-0)} = 18$; for Gal1 and Gal2 we use $L'_{CO(5-4)}/L'_{CO(1-0)} = 8.4$. These values are in line with the ones measured for objects observed in literature, which have similar $SL_{5/4}$ slopes (see Figure 4 in Carilli & Walter 2013 for a
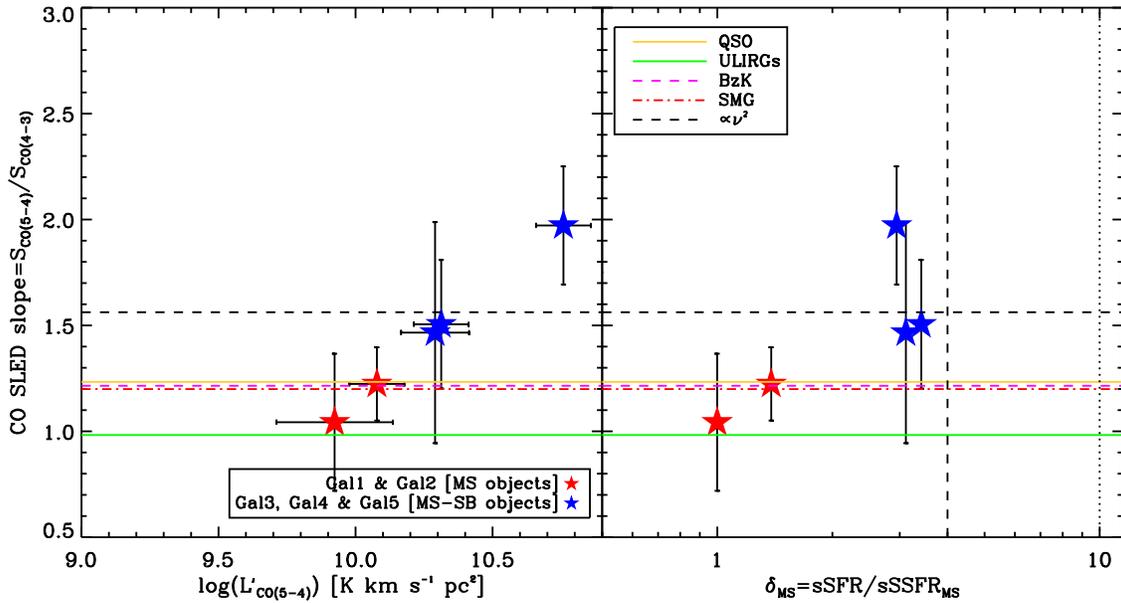
Figure 5. CO SLED slope between CO (5−4) and CO (4−3), defined as $S_{CO(5-4)}/S_{CO(4-3)}$, as a function of the CO (5−4) luminosity $L'_{CO(5-4)}$ (left panel) and of δ_{MS} (right panel; for clarity here we show the value obtained using the SFR derived by MAGPHYS only, but the result does not change if we use the SFR derived from the FIR), for the five galaxies in the sample. The colored horizontal lines show the average SLED slope for different classes of objects: solid yellow for the median of the QSOs from Carilli & Walter (their Figure 4), dotted–dashed red for SMGs (Bothwell et al. 2013), dashed magenta for BzK (Daddi et al. 2015), and green for local ULIRGs (Papadopoulos et al. 2012). The dashed horizontal line shows the slope for the case of constant brightness temperature on the Rayleigh–Jeans scale, i.e., $S \propto \nu^2$. The vertical lines in the left panel highlight the loci 4× and 10× above the MS. The two galaxies that are closer to the MS (Gal1 and Gal2) are shown with red stars, while the three that are at the boundary between MS and starbursts are shown in blue. Error bars are estimated by propagating the errors on the individual fluxes to the ratio.

compilation): M82, for example, has $L'_{CO(5-4)}/L'_{CO(1-0)} \sim 20$, and BzKs have $L'_{CO(5-4)}/L'_{CO(1-0)} \sim 6.5$, not far from the factors that we used here.

For the α_{CO} conversion factor we instead decided to use a single value for all galaxies, and we chose the metallicity-dependent α_{CO} factor suggested by Tacconi et al. (2018) for galaxies on the MS: applying their Equations (2) and (4) at the median redshift of our sample, for a stellar mass of $10^{10.5} M_\odot$, we obtain $\alpha_{CO} = 3.8\ M_\odot(\mathrm{K\ km\ s^{-1}\ pc^{-2}})^{-1}$.

In order to obtain an estimate of the gas mass from the dust continuum in the Rayleigh–Jeans regime, we apply the method by Groves et al. (2015), which provides calibrations of the gas mass–dust luminosity relation at different wavelengths. Our band 4 observations probe the continuum very close to the 500 μm rest frame; therefore, we use the calibration at that wavelength. However, since the tuning of ALMA observations is different for each object, and in addition they are at slightly different redshifts, the band 4 observations correspond to slightly different rest-frame wavelengths, between ∼480 and ∼550 μm rest frame: in order to account for that, we correct the observed fluxes by extrapolating along the $F \propto \lambda^{-4}$ Rayleigh–Jeans law, from the observed wavelength to exactly 500 μm; the corrections are between 0.7 and 1.15. We then convert fluxes to luminosities and use the conversion in Groves calibrated for galaxies with $M/M_* > 10^9$ to obtain gas masses.

We report the molecular gas masses that we obtain with these two procedures in Table 4: they range from ∼9 × 10^{10} to 2.2 × $10^{11} M_\odot$, implying very high molecular gas fractions $\mu_{gas} = M_{gas}/(M_{gas} + M_*)$, between 65% and 80%. We also estimate the gas depletion times $t_{depl} = M_{gas}/SFR$, using the SFR estimated by MAGPHYS: we obtain values in the range 0.2 Gyr < t_{depl} < 1 Gyr. Both f_{gas} and t_{depl} are given in Table 4. In Figure 6 we compare the molecular gas estimated via the

CO line and dust continuum: only for two out of five objects in the sample do the two estimates agree, within the errors. It is interesting to note that these two objects have very similar dust temperatures to those estimated by MAGPHYS, around $T_{dust} \sim 45$ K; the two objects for which the dust is colder (with $T_{dust} \sim 35-40$ K) are those for which the dust-based gas mass is larger than the CO one; and conversely, the object with warmer dust temperature ($T_{dust} \sim 60$ K) is the one for which the dust-based gas mass is smaller than the CO one. In the same figure, we use different symbols to see if this trend could be driven by the distance from the MS δ_{MS}, but it does not seem to be the case: the three galaxies that lie closer to the MS–SB separation are equally above, on, and below the diagonal in Figure 6. Summarizing, this could imply that the calibration to obtain gas mass from the 500 μm rest-frame flux gives estimates that are closer to the ones from the CO for galaxies with dust temperatures around 35–40 K; for galaxies with warmer (colder) dust temperature, the dust emission would be shifted toward lower (larger) wavelengths, the flux in the Rayleigh–Jeans regime would decrease (increase), and one would get a smaller (larger) flux and therefore a smaller (larger) gas mass.

In Figure 7 we show μ_{gas} and t_{depl} as a function of redshift, together with the values for MS galaxies by Dessauges-Zavadsky et al. (2015, 2017), who compiled a list of star-forming galaxies with 0.3 < sSFR/sSFR$_{MS}$ < 3 for which a determination of the molecular gas mass was available based on CO line measurements. Our data almost double the number of molecular gas measurements at 3 < z < 3.4, in a range where most of the available measurements are for lensed systems (four out of five galaxies in Dessauges-Zavadsky et al. 2017). Our derived gas fractions are all above the best-fit curve $f_{gas} = 1/(1 + (0.12 \times (1+z)^{1.95})^{-1})$ by Dessauges-Zavadsky et al. (2017), but probably their best fit is somewhat
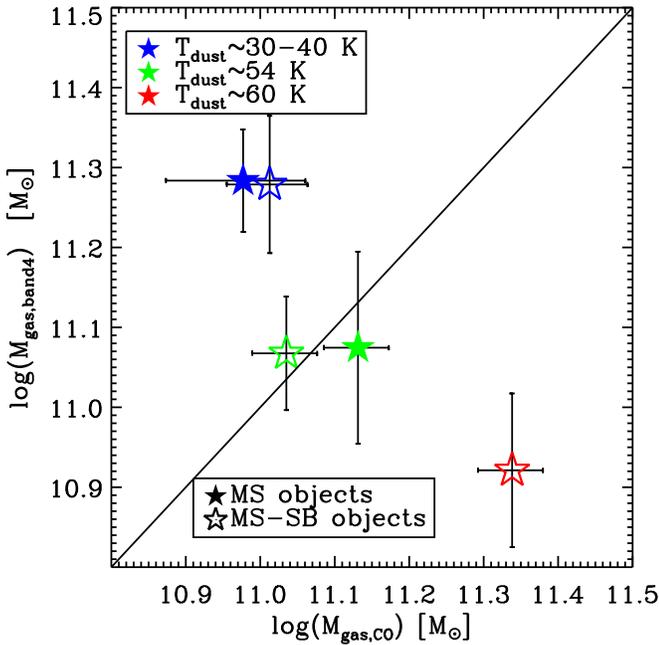
Figure 6. Comparison of the molecular gas mass estimated via the CO and dust continuum. Different colors indicate different dust temperatures, as estimated by MAGPHYS; filled symbols show the two galaxies that are closer to the MS, while the open ones show the three galaxies that lie close to the boundary with the SB sequence.

biased low at $z > 2.8$ by the lone outlier that has a very low gas fraction. Otherwise, our objects lie in the same region at $0.6 < f_{gas} < 0.8$ as the other galaxies by Dessauges-Zavadsky et al. (2017). Our measurements then confirm the increase in gas fractions of MS galaxies at $z > 2$ that was hinted at by previous observations. The depletion times for our five galaxies are also comparable to the measurements from Dessauges-Zavadsky et al. (2017) in the same redshift range and distribute quite well around the best-fit curve $t_{depl} = 1.15 \times (1 + z)^{-0.85}$ by Dessauges-Zavadsky et al. (2017), confirming the observed decrease of t_{depl} with redshift.

In Figure 7 we report also the predictions of the 2-SFM model by Sargent et al. (2014), for a galaxy of $4 \times 10^{10} \, M_\odot$ (average stellar mass in our sample), lying exactly on the MS, or 3 times above it (the median δ_{MS} of our sample). These predictions are based on the combination of two scaling relations: (i) the evolution of the star-forming MS, and (ii) the integrated Schmidt–Kennicutt relation (assuming that it does not evolve with redshift). In this framework, these curves provide a zero-level physical interpretation of the evolutionary trends and the position galaxies in both panels. It is interesting that all five galaxies in the sample have quite similar gas fractions (also the gas masses span a range of 0.3 dex only), and they all lie in the region of the f_{gas} versus z plane composed between the prediction for the average MS and 3 times above it: this indicates that they have f_{gas} fractions in line with the prediction of the model for MS galaxies at that redshift. On the other hand, the five galaxies have more spread-out values of the gas depletion timescales: the two galaxies that lie closer to the average MS (Gal1 and Gal2) have t_{depl} quite longer than the other three galaxies, and they lie closer to the prediction for average MS galaxies; the other three have smaller t_{depl}, closer to (and beyond) the prediction for galaxies 3 times above the average MS.
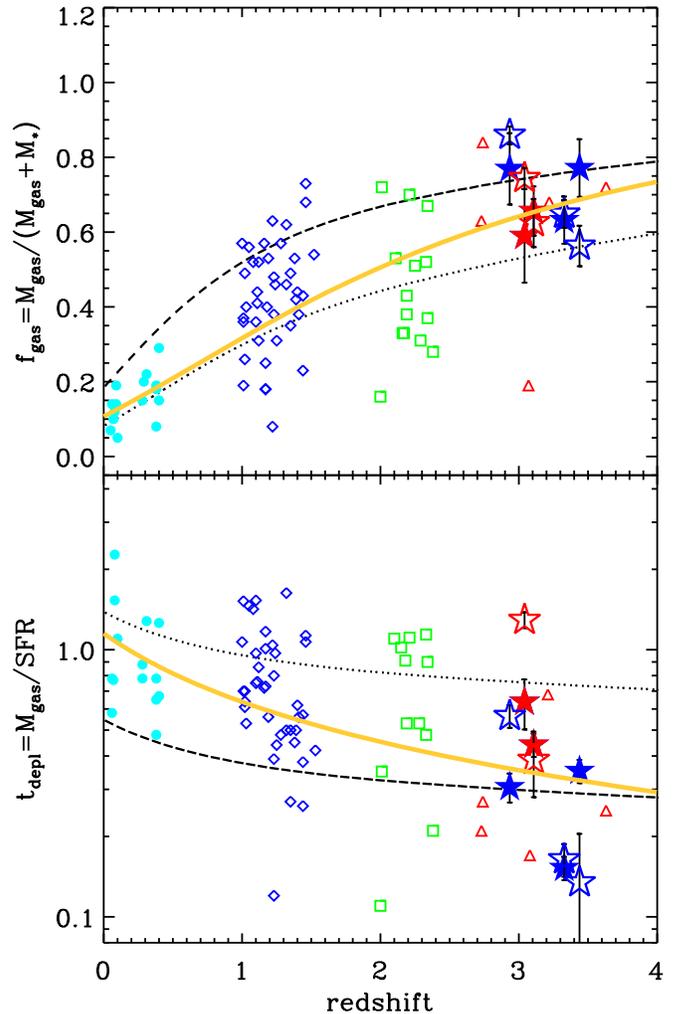

Figure 7. As a function of redshift, gas fraction (top panel) and gas depletion time (bottom panel) for the five galaxies in our sample. Red stars indicate the two galaxies closer to the MS, the blue stars indicate the objects at the boundary with the SBs, respectively, and filled and open stars indicate measurements with gas masses obtained through CO and band 4 continuum, respectively. We also show measurements from the literature by Dessauges-Zavadsky et al. (2015, 2017), for MS galaxies, divided into redshift bins: cyan at $z < 0.5$, blue at $1 < z < 1.5$, green at $2 < z < 2.5$, and red at $2.8 < z < 3.5$. The dotted and dashed lines indicate the predictions of the 2-SFM model by Sargent et al. (2014) for a galaxy with stellar mass $4 \times 10^{10} \, M_\odot$ lying exactly on the average MS or a factor of 3 above the MS, respectively. The solid orange line indicates the fits to the data proposed by Dessauges-Zavadsky et al. (2017): $f_{gas} = 1/(1 + (0.12 \times (1 + z)^{1.95})^{-1})$ and $t_{depl} = 1.15 \times (1 + z)^{-0.85}$.

6. Dynamical Masses and α_{CO}

In order to obtain an estimate of the dynamical masses of our objects, we apply the method outlined by Wang et al. (2013) and applied among others by Capak et al. (2015): $M_{dyn} = 1.16 \times 10^5 V_{cir}^2 D$, where V_{cir} is the circular velocity in km s^{-1} and D is the diameter in kpc. The circular velocity is assumed to be $V_{cir} = 1.763 \, \sigma_{CO(5-4)} / \sin(i)$, where $\sigma_{CO(5-4)}$ is the velocity dispersion and i is the disk inclination angle. We estimated the inclination angle from the ALMA images, presented in Figure 2, as $i = \cos^{-1}(b/a)$: the axial ratio that we used is the one calculated on the deconvolved sizes, and the inclinations that we obtain range between $i = 45°$ and $i = 60°$. For Gal2, for which the emission in both CO lines is unresolved, we assumed $i = 57°$, the most probable value in
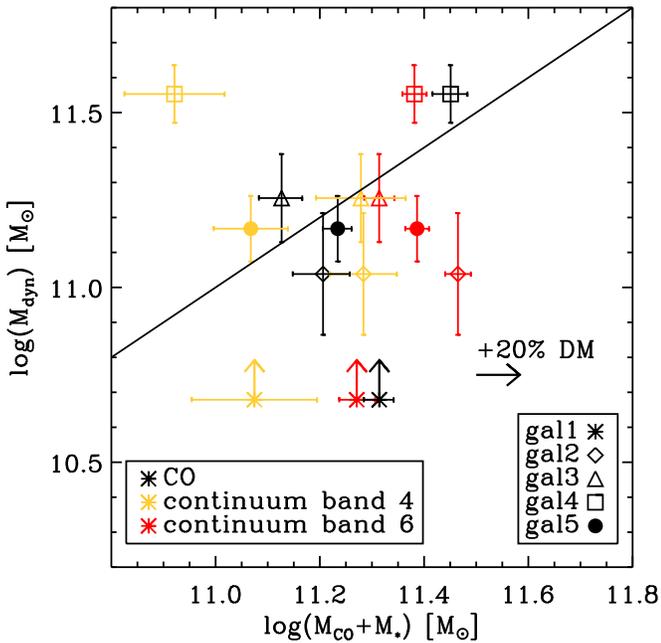
Figure 8. Comparison between dynamical mass and the sum of gas mass and stellar mass, for different methods to constrain the gas mass: black, red, and orange symbols indicate the values based on CO, continuum in band 4 at 240 GHz, and continuum in band 4 at 140 GHz, respectively. The gas masses based on CO are obtained using $\alpha_{\rm CO} = 3.8\ M_\odot({\rm K\ km\ s^{-1}\ pc^{-2}})^{-1}$, the value suggested by Tacconi et al. (2018) at the median redshift of our sample for galaxies of similar stellar mass. The dynamical mass obtained for Gal1 is indicated as a lower limit, as the true inclination is probably much smaller than the one we obtained from the ALMA images. The rightward-pointing arrow above the legend shows the total mass increase should 20% of DM be added.

case of random orientation. This method provides a good first guess of the dynamical mass, but it suffers from the quite large uncertainties on the size and axial ratio, which cannot be constrained very robustly, due to the limited spatial resolution and the elongation of the beam for some of our ALMA observations. We report the dynamical masses in Table 4; moreover, in Figure 8 we compare $M_{\rm dyn}$ with the sum of stellar mass M_* and gas mass $M_{\rm gas}$, for gas masses based on different techniques (converting the CO line luminosity, and from the continuum in bands 4 and 6).

It is interesting to note that the measurements from CO scatter quite nicely around the 1:1 relation, apart from Gal1, which has a very small velocity dispersion $\sigma_{\rm CO(5-4)}$, leading to a very small $M_{\rm dyn}$ (it is quite possible that the axial ratio for this object is poorly estimated, as the beam of the band4 observations is quite elongated and could have led to an overestimation of i; therefore, we indicate its dynamical mass as a lower limit). We did not include any dark matter (DM) in these calculations, to simplify the interpretation; however, a DM fraction of 20% (similar to the one observed by Genzel et al. 2017 and Lang et al. 2017 in galaxies of similar stellar mass at $z \sim 2$) would only slightly increase the total mass (see the arrow in Figure 8). This implies that the mass bound in stars, plus the mass in the cold gas phase (also in the case in which we added 20% of DM), is comparable to the dynamical mass in these galaxies. This suggests that all the assumptions we made in constraining the dynamical mass and the molecular gas mass are at least reasonable. In particular, it is reasonable to assume a common value for $\alpha_{\rm CO}$ for all galaxies, with a value that is typical of MS galaxies: for example, having assumed an $\alpha_{\rm CO}$ value more typical of starburst galaxies, $\alpha_{\rm CO} = 0.8\ M_\odot({\rm K\ km\ s^{-1}\ pc^{-2}})^{-1}$, would have led to total masses more than 3 times smaller than the

dynamical ones: with the velocity dispersions that we observe, the only way to decrease the dynamical masses by a similar amount to reconcile them with the total gas+star masses would be to assume that our galaxies are seen almost edge-on, an assumption that is not at all supported by the observations.

This comparison provides at least a first constraint on the $\alpha_{\rm CO}$ parameter for MS galaxies at $3 < z < 3.5$: the value that we assumed using the recipe provided by Tacconi et al. (2018), based mainly on continuum-derived molecular gas masses, turns out to be the one that is needed to obtain a total mass that matches the dynamical mass. Even assuming that the inclination angle is overestimated for all galaxies, that would mean that the true dynamical masses would be even larger, and we would need a larger $\alpha_{\rm CO}$ factor to recover the total dynamical mass, or a substantial amount of DM.

As a check, in Figure 8 we also compared the total dynamical mass to the sum of stellar and gas mass, if the continuum in the Rayleigh–Jeans regime is used as a tracer of the molecular gas mass (similar to Scoville et al. 2014, 2016; Groves et al. 2015). In particular, we used the gas masses published by Schinnerer et al. (2016), based on the continuum observed at 240 GHz in band 6 for these same five objects, and we calculated also the masses using the continuum in band 4 at 140 GHz, already presented in Section 5. The difference between CO and continuum-based gas masses is already presented in Figure 6: galaxies with colder (warmer) dust tend to have larger (smaller) dust-based gas masses. It can be seen that the gas masses based on CO are the ones that give the best agreement with the dynamical masses; the continuum in band 4 seems to provide reasonable estimates for Gal2, Gal3, and Gal5, but not for Gal4, which is the galaxy with the warmest dust and therefore the smallest dust-continuum-based gas mass; the continuum in band 6 provides a good estimate for Gal4 but seems to give too large molecular gas masses for the other objects. It is important to stress that this sample is the first at $z > 3$ for which the different methods to constrain the gas mass can be compared: although the sample is quite small, it is clear that the three techniques give results that are not that far from each other.

7. Summary

In this paper we presented ALMA observations of two CO mid-high transitions for a sample of five star-forming galaxies across the MS at $3 < z < 3.5$. Two of them lie very close to the average MS, as constrained by Schreiber et al. (2015); the remaining three lie at the boundary between MS and SBs. For all objects we detected the CO (5−4) transition at more than 7σ, and we detected a lower CO transition (CO (4−3) for four objects and CO (3−2) for the remaining one) at more than 3σ. In addition, we also detected the continuum in band 4, at $\sim$140 GHz, corresponding to 500 μm rest frame, at better than 4σ. These five new detections double the number of star-forming galaxies with multiple CO detections in a region of the sSFR/sSFR$_{\rm MS}$ versus redshift plane that is so far scarcely populated, and where most of the objects studied so far are lenses (see Figure 1).

Our main findings are as follows:

1. From a multiwavelength spectrophotometric analysis, the galaxies in our sample have similar properties to normal star-forming galaxies at $z > 3$: they span the upper half of the star-forming MS, a region that is populated by the less

star-forming among the SMGs and galaxies selected through the BzK technique (Figure 1). They display modest but significant spatial offsets between the position of the UV rest-frame emission and the dust component, indicating a large amount of dust that is not homogeneously distributed in the galaxies, blocking UV radiation along some lines of sight while letting it through others. In general, the stellar component is more aligned with the dust continuum, as is expected since optical light is less attenuated than UV light. The CO emission is in general aligned with the stellar and dust emission, indicating that molecular gas and dust are well mixed. Only for one object, Gal2, do we find a different configuration: the dust emission, traced by the ALMA continuum, comes from two distinct regions, while we detect CO only in the southernmost of the two (and we stress that the ALMA tuning could detect CO also in the north one, if CO were present and excited as in the south one).

2. We find a positive correlation between $L'_{CO(5-4)}$ and L_{FIR} for our five galaxies at $z \sim 3$, confirming that the correlation that is observed at lower redshifts (Daddi et al. 2015; Liu et al. 2015) also holds for MS galaxies at $z \sim 3$. The two galaxies that lie closer to the average MS at that redshift, which have also smaller SFR, are the ones with fainter $L'_{CO(5-4)}$ luminosities. These findings support the claim that the CO (5−4) luminosity can be used by as an independent star formation indicator, as suggested by Daddi et al. (2015).

3. We find a correlation between three quantities: the CO SLED slope between CO (5−4) and CO (4−3), the $L'_{CO(5-4)}$ luminosity, and the distance from the MS δ_{MS} (see Figure 5): the two objects that lie closer to the MS have slopes similar to BzKs and SMGs and have faint CO (5−4) luminosities. This indicates that the two former objects are likely normal MS galaxies that form stars in a secular mode, with large gas reservoirs and long gas depletion timescales (see Table 4 and Figure 7). The other three, which lie closer to the starburst region, have definitely peculiar CO SLEDs: a possibility is that the molecular gas in these galaxies is in multiple phases, with the denser gas undergoing a very active star-forming episode, therefore emitting an excess of CO (5−4) photons with respect to the less dense gas.

4. We find systematic differences in the molecular gas mass estimate when the CO SLED is used as opposed to the dust continuum in the Rayleigh–Jeans regime (Figure 4): gas masses derived from the CO are larger (smaller) than dust-based ones for galaxies with warmer (colder) dust temperature, and they agree for galaxies with dust temperatures $T \sim 54$ K, as estimated by the MAGPHYS SED fitting.

5. We also showed that constraining the slope of the CO SLED can help to at least reduce the uncertainties when extrapolating the SLED down to CO (1−0) to trace the molecular gas mass: by doing so, and then assuming a conversion factor $\alpha_{CO} = 3.8 \, M_{\odot}(\text{K km s}^{-1} \text{ pc}^{-2})^{-1}$, typical for star-forming galaxies on the MS (Tacconi et al. 2018), we find that our five galaxies are very gas-rich, with gas fractions between 60% and 80%, values that are very close to the ones measured for similar (but lensed) galaxies in the same redshift regime (Dessauges-Zavadsky et al. 2017). This

puts on firmer grounds the findings in literature that the increase in gas fraction slightly flattens out at $z > 3$ (Schinnerer et al. 2016; Dessauges-Zavadsky et al. 2017). On the other hand, we find also that these galaxies have depletion times in the range 0.2 Gyr $< t_{depl} < 1$ Gyr, again similar to the values found in the literature for similar MS galaxies at $z \sim 3$ (Dessauges-Zavadsky et al. 2017, but mainly for lensed galaxies). We also find that the two galaxies that lie close to the average MS have longer gas depletion timescales than the ones that lie at the boundary to starbursts: this suggests that the depletion times decrease moving up perpendicular to the MS, similar to what has been found by Schinnerer et al. (2016) using dust as a gas mass tracer.

6. We obtain a first estimate of the dynamical masses, using common assumptions, which turn out to be comparable to the total *baryonic* mass (stellar + gas) in these galaxies, except for one galaxy, which is probably observed almost face-on. This is important because it demonstrates that the assumptions we made to constrain the molecular gas mass and the dynamical mass from the CO lines are reasonable. Moreover, it allows us, for the first time at these redshifts, to put an observational constraint on the α_{CO} parameter, which turns out to be very close to the value of $\alpha_{CO} = 3.8 \, M_{\odot}(\text{K km s}^{-1} \text{ pc}^{-2})^{-1}$ prescribed by Tacconi et al. (2018) for normal star-forming galaxies.

ORCID iDs

Paolo Cassata https://orcid.org/0000-0002-6716-4400
Daizhong Liu https://orcid.org/0000-0001-9773-7479
Brent Groves https://orcid.org/0000-0002-9768-0246
Eva Schinnerer https://orcid.org/0000-0002-3933-7677
Mark Sargent https://orcid.org/0000-0003-1033-9684
Alexander Karim https://orcid.org/0000-0002-8414-9579
Margherita Talia https://orcid.org/0000-0003-4352-2063
Olivier Le Fèvre https://orcid.org/0000-0001-5891-2596
Brian C. Lemaux https://orcid.org/0000-0002-1428-7036
Michael Romano https://orcid.org/0000-0002-9948-3916
Chiara Mancini https://orcid.org/0000-0002-4297-0561
Laura Morselli https://orcid.org/0000-0003-0753-2571
Giulia Rodighiero https://orcid.org/0000-0002-9415-2296
Lucía Rodríguez-Muñoz https://orcid.org/0000-0002-0192-5131

Andrea Enia ⓘ https://orcid.org/0000-0002-0200-2857
Vernesa Smolcic ⓘ https://orcid.org/0000-0002-3893-8614

References

Bolatto, A. D., Wolfire, M., & Leroy, A. K. 2013, ARA&A, 51, 207
Bothwell, M. S., Smail, I., Chapman, S. C., et al. 2013, MNRAS, 429, 3047
Briggs, D. S. 1995, AAS Meeting Abstracts, 27, 1444
Capak, P., Aussel, H., Ajiki, M., et al. 2007, ApJS, 172, 99
Capak, P., Carilli, C., Jones, G., et al. 2015, Natur, 522, 455
Carilli, C., & Walter, F. 2013, ARA&A, 51, 105
Cassata, P., Morselli, L., Faisst, A., et al. 2020, arXiv:2002.00967
Combes, F. 2016, From Interstellar Clouds to Star-forming Galaxies: Universal
    Processes? (Cambridge: Cambridge Univ. Press), 240
Cucciati, O., Tresse, L., Ilbert, O., et al. 2012, A&A, 539, 31
da Cunha, E., Charlot, S., & Elbaz, D. 2008, MNRAS, 388, 1595
da Cunha, E., Charmandaris, V., Díaz-Santos, T., et al. 2010, A&A, 523, 78
Daddi, E., Bournaud, F., Walter, F., et al. 2010, ApJ, 713, 686
Daddi, E., Dannerbauer, H., Elbaz, D., et al. 2008, ApJ, 673, 21
Daddi, E., Dannerbauer, H., Liu, D., et al. 2015, A&A, 577, 46
Daddi, E., Dickinson, M., Morrison, G., et al. 2007, ApJ, 670, 156
Dessauges-Zavadsky, M., Zamojski, M., Rujopakarn, W., et al. 2017, A&A,
    605, 81
Dessauges-Zavadsky, M., Zamojski, M., Schaerer, D., et al. 2015, A&A,
    577, 50
Elbaz, D., Leiton, R., Nagar, N., et al. 2018, A&A, 616, 110
Erb, D. K., Steidel, C. C., Trainor, R. F., et al. 2014, ApJ, 795, 33
Faisst, A. L., Capak, P., & Hsieh, B. C. 2016, ApJ, 821, 122
Geach, J. E., Smail, I., Moran, S. M., et al. 2011, ApJ, 730, 19
Genzel, R., Förster-Schreiber, N. M., Übler, H., et al. 2017, Natur, 543, 397
Genzel, R., Tacconi, L. J., Lutz, D., et al. 2015, ApJ, 800, 20
Greve, T. R., Bertoldi, F., Smail, I., et al. 2005, MNRAS, 359, 1165
Groves, B. A., Schinnerer, E., Leroy, A., et al. 2015, ApJ, 799, 96
Hildebrand, R. H. 1983, QJRAS, 24, 267
Jin, S., Daddi, E., Liu, D., et al. 2018, ApJ, 864, 56
Kennicutt, R. C., Jr. 1998, ARA&A, 36, 189
Koekemoer, A. M., Aussel, H., Calzetti, D., et al. 2007, ApJS, 172, 196
Laigle, C., McCracken, H. J., Ilbert, O., et al. 2016, ApJS, 224, 24
Lang, P., Förster Schreiber, N. M., Genzel, R., et al. 2017, ApJ, 840, 92
Le Fèvre, O., Tasca, L. A. M., Cassata, P., et al. 2015, A&A, 576, 79

Lilly, S. J., Le Fèvre, O., Renzini, A., et al. 2007, ApJS, 172, 70
Liu, D., Schinnerer, E., Groves, B., et al. 2019, ApJ, 887, 235
Liu, Daizhong., Gao, Yu., Isaak, K., et al. 2015, ApJ, 810, 14
Madau, P., & Dickinson, M. 2014, ARA&A, 52, 415
Magdis, G. E., Daddi, E., Béthermin, M., et al. 2012a, ApJ, 760, 6
Magdis, G. E., Daddi, E., Sargent, M., et al. 2012b, ApJ, 758, 9
Magnelli, B., Saintonge, A., Lutz, D., et al. 2012, A&A, 548, 22
Marchi, F., Pentericci, L., Guaita, L., et al. 2019, A&A, 631, 19
McCracken, H. J., Milvang-Jensen, B., Dunlop, J., et al. 2012, A&A, 544, 156
McMullin, J. P., Waters, B., Schiebel, D., et al. 2007, in ASP Conf. Ser. 376,
    Astronomical Data Analysis Software and Systems XVI, ed. R. A. Shaw,
    F. Hill, & D. J. Bell (San Francisco, CA: ASP), 127
Narayanan, D., & Krumholz, M. R. 2014, MNRAS, 442, 1411
Noeske, K. G., Weiner, B. J., Faber, S. M., et al. 2007, ApJ, 660, 43
Papadopoulos, P. P., van der Werf, P., Xilouris, E., et al. 2012, ApJ, 751, 10
Rodighiero, G., Daddi, E., Baronchelli, I., et al. 2011, ApJL, 739, L40
Rodighiero, G., Renzini, A., Daddi, E., et al. 2014, MNRAS, 443, 19
Saintonge, A., Kauffman, G., Wang, J., et al. 2011, MNRAS, 415, 61
Saintonge, A., Lutz, D., Genzel, R., et al. 2013, ApJ, 778, 2
Sanders, D. B., Salvato, M., Aussel, H., et al. 2007, ApJS, 172, 86
Sargent, M., Daddi, E., Béthermin, M., et al. 2014, ApJ, 793, 19
Schinnerer, E., Groves, B., Sargent, M. T., et al. 2016, ApJ, 833, 112
Schreiber, C., Elbaz, D., Pannella, M., et al. 2016, A&A, 589, 35
Schreiber, C., Pannella, M., Elbaz, D., et al. 2015, A&A, 575, 74
Scoville, N., Aussel, H., Brusa, M., et al. 2007, ApJS, 172, 1
Scoville, N., Aussel, H., Sheth, K., et al. 2014, ApJ, 783, 84
Scoville, N., Sheth, K., Aussel, H., et al. 2016, ApJ, 820, 83
Sharon, C. E., Riechers, D. A., Hodge, J., et al. 2016, ApJ, 827, 18
Solomon, P. M., Downes, D., & Radford, S. J. E. 1992, ApJ, 398, 29
Steidel, C. C., Erb, D. K., Shapley, A. E., et al. 2010, ApJ, 717, 289
Tacconi, L. J., Genzel, R., Neri, R., et al. 2010, Natur, 463, 781
Tacconi, L. J., Genzel, R., Saintonge, A., et al. 2018, ApJ, 853, 179
Tacconi, L. J., Genzel, R., Smail, I., et al. 2008, ApJ, 680, 246
Tacconi, L. J., Neri, R., Chapman, S. C., et al. 2006, ApJ, 640, 228
Tacconi, L. J., Neri, R., Genzel, R., et al. 2013, ApJ, 768, 74
Tasca, L., Le Fèvre, O., Hathi, N. P., et al. 2015, A&A, 581, 54
Tomczak, A. R., Quadri, R. F., Tran, K.-V. H., et al. 2016, ApJ, 87, 118
Villanueva, V., Ibar, E., Hughes, T. M., et al. 2017, MNRAS, 470, 3775
Wang, R., Wagg, J., Carilli, C., et al. 2013, ApJ, 773, 44
Whitaker, K. E., van Dokkum, P. G., Brammer, G., & Franx, M. 2012, ApJ,
    754, 29